

# Granular Aluminum Parametric Amplifier for Low-Noise Measurements in Tesla Fields

Nicolas Zapata,<sup>1,\*</sup> Ivan Takmakov,<sup>1,2,3</sup> Simon Günzler,<sup>1,2</sup> Ameya Nambisan,<sup>1</sup>  
Dennis Rieger,<sup>2</sup> Thomas Reisinger,<sup>1</sup> Wolfgang Wernsdorfer,<sup>1,2</sup> and Ioan M. Pop<sup>1,2,4,†</sup>

<sup>1</sup>*IQMT, Karlsruhe Institute of Technology, 76131 Karlsruhe, Germany*

<sup>2</sup>*PHI, Karlsruhe Institute of Technology, 76131 Karlsruhe, Germany*

<sup>3</sup>*Current address: IQM Quantum Computers, Espoo 02150, Finland*

<sup>4</sup>*Physics Institute 1, Stuttgart University, 70569 Stuttgart, Germany*

(Dated: March 19, 2024)

Josephson junction parametric amplifiers have become essential tools for microwave quantum circuit readout with minimal added noise. Even after improving at an impressive rate in the last decade, they remain vulnerable to magnetic fields, which limits their use in many applications such as spin qubits, Andreev and molecular magnet devices, dark matter searches, etc. Kinetic inductance materials, such as granular aluminum (grAl), offer an alternative source of non-linearity with innate resilience to in-plane magnetic fields. We present a non-degenerate amplifier made of two coupled grAl resonators resilient to in-plane magnetic field up to 1 T. It operates close to the quantum limit at 20 dB amplification, with 28 MHz gain-bandwidth product and -110 dBm saturation power.

The remarkable progress in Josephson junction (JJ) based parametric amplifiers has sparked their widespread adoption in both academic and industrial research groups, establishing single-shot quantum state detection of superconducting qubits as an integral capability in circuit quantum electrodynamics [1–4]. State-of-the-art amplifiers are essential for the measurement of syndromes during error correction of superconducting quantum registers [5–8], they enable the development of novel detection techniques [9–13], and they serve as indispensable instruments to uncover microscopic mechanisms degrading superconducting qubit coherence [14–16]. However, the magnetic field induced Fraunhofer pattern for the JJ critical current [17–19] constrains their applicability in systems such as spin [12, 20, 21] and Andreev qubits [22, 23], spin ensembles [24, 25], molecular magnet devices [26] and dark matter detectors [27–29].

Recent experiments have used magnetic shielding to protect JJ-based amplifiers [12, 21, 30], but this comes at the price of placing the amplifier farther from the measured device, risking to introduce losses and reduce the readout quantum efficiency. Ideally, one would use a magnetic field resilient amplifier directly coupled to the device under test; several platforms have recently been developed to achieve this goal. Among these, implementations based on graphene junctions [31, 32] and proximitized semiconductors [33, 34] have demonstrated 20 dB of gain and operation close to the quantum limit. However, technologically involved fabrication makes it challenging to integrate them in more complex systems and their relatively low saturation power (-130 to -120 dBm) limits the readout signal amplitude. An alternative path employs the non-linearity of kinetic inductance materials like NbN [35, 36], NbTiN [37–40] or granular aluminum (grAl) [41, 42], which offer magnetic field resilience, adaptable integration and larger dynamic range.

Remarkable progress has recently been reported for NbN amplifiers, which have been proven to operate in fields up to 6 T [36] and close to the quantum limit up to 0.5 T [35]. This required pushing the boundaries of device engineering and the deposition of nm-thin films to increase the non-linearity to values comparable to JJ-based implementations. Even though NbN has enabled these achievements, its relatively large critical current density, in the range of mA/ $\mu\text{m}^2$ , limits its non-linearity compared to grAl. Two orders of magnitude lower critical current densities can readily be achieved in grAl films, which has enabled devices with amenable non-linearity from mHz to GHz [41, 43, 44], while still remaining an order of magnitude below the superconducting-to-insulator transition (SIT) resistivity threshold. This flexibility relaxes device volume engineering requirements and it opens the door for new classes of devices. An additional order of magnitude in non-linearity could be gained close to the grAl SIT, however, the emergence of complex physical phenomena might hinder device performance [45–48].

In this work we tailor the non-linearity of grAl to fabricate a standing wave parametric amplifier (grAIPA), which operates near the quantum limit in magnetic fields up to 1 T in-plane. Following the approach of Refs. [49, 50] for JJ amplifiers, we implement a grAl Bose-Hubbard dimer which employs 4-wave mixing to produce phase preserving amplification, where the signal and idler are separated in different modes. We obtain 20 dB amplification, with 28 MHz gain-bandwidth product and 0.1 GHz signal-to-pump detuning. Moreover, by targeting the non-linearity of the amplifier between 1-3 kHz, we achieve a saturation power of -110 dBm, covering the typical power range for quantum device readout. These features make grAIPAs convenient and powerful tools, ready to be integrated and to extend the range of applications which benefit from quantum limited readout.

The grAIPA amplifier, operated in reflection, consists of two capacitively coupled grAl resonators mounted in a single-port cylindrical waveguide, coupled via evanescent electric field to a coaxial cable (cf. Fig. 1(a)). The res-

\* nicolas.gonzalez2@kit.edu

† ioan.pop@kit.edu

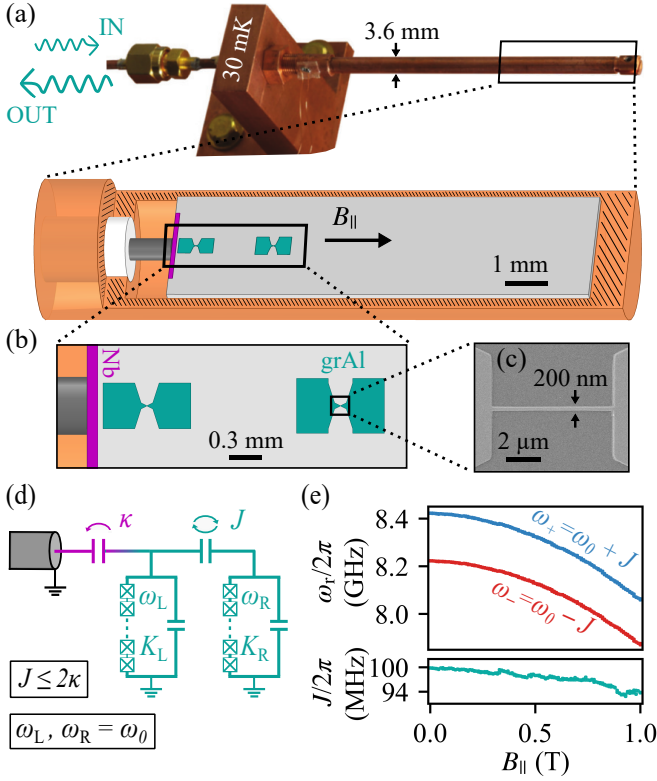


Figure 1. **Device design and frequency dependence in magnetic field up to 1 T.** (a) Photograph (top) and schematics (bottom) of the sample holder used for microwave reflection measurements, similar to Refs. [42, 44, 51]. (b) The granular Aluminum Parametric Amplifier (grAlPA) consists of a pair of lumped-element grAl resonators (green), comprised of two coplanar capacitor plates connected by a central strip. To stabilize the evanescent field coupling of the grAlPA to the coaxial central pin (black) we add a Nb pad (purple) at the edge of the substrate (see Appendix C). (c) Scanning electron beam image of the central grAl nanostructure. (d) Equivalent circuit diagram of the grAlPA. The design resembles a Bose-Hubbard dimer, similar to Refs. [49, 50]. The grAl strip shown in (c) can be modeled as an array of Josephson Junctions [41, 52] with a self-Kerr non-linearity denoted as  $K_i$  ( $i = R, L$ ). The hopping interaction  $J$  gives rise to a pair of hybridized modes  $\omega_{\pm}$ . (e) Measured frequency dependence of the dimer  $\omega_{\pm}$  (top) and hopping interaction  $J$  (bottom) as a function of in-plane magnetic field up to 1 T. The magnetic field is aligned with the symmetry axis of the waveguide, as shown in (a).

onators are formed by two coplanar capacitor plates connected by a central grAl strip, as illustrated in Fig. 1(b) and (c). The grAl strip gives 80% of the total inductance (see Appendix A). The size of each capacitor plate is chosen to match the frequencies of the two modes and obtain perfect hybridization. The device is fabricated in a single step of electron beam lithography, followed by 0-angle evaporation on a c-plane sapphire substrate (see Appendix B). We deposit a 40 nm grAl film of resistivity  $830 \mu\Omega\text{cm}$ , which gives a kinetic inductance

$L_K = 0.12 \text{ nH}/\square$  and 4.2 nH of strip inductance.

The waveguide provides a clean microwave environment for the grAlPA thanks to its  $\approx 60 \text{ GHz}$  cut-off frequency, a factor of five above the frequency range commonly used in superconducting devices. Moreover, the evanescent coupling eliminates the need for potentially lossy and noisy wire bonds. The challenge when using this strategy arises from the exponential susceptibility of the coupling to variations in the distance between the pin and the grAlPA. In order to mitigate this effect we add a  $40 \mu\text{m}$  wide and  $40 \text{ nm}$  thick Nb pad at the edge of the chip, between the coaxial cable and the grAlPA, using optical lithography. The Nb coupling pad acts as an on-chip extension of the central pin of the coaxial cable, uniformly spreading the electric field lines (see Appendix C).

Figure 1(d) shows the equivalent grAlPA circuit, which can be modeled by the following Bose-Hubbard-dimer Hamiltonian [49, 50, 53]:

$$H/\hbar = \sum_{i=L,R} \left( \omega_i a_i^\dagger a_i + \frac{K_i}{2} a_i^\dagger a_i^\dagger a_i a_i \right) + J a_L^\dagger a_R + \text{h.c.}, \quad (1)$$

where the two bosonic modes  $a_i$ , with  $i = L, R$ , correspond to the left and right grAl resonators, respectively. The individual resonant frequencies are  $\omega_i$ , the on-site potentials  $K_i$  are given by the first-order Kerr non-linearity of the central grAl strips, and the hopping term  $J$  arises from the electric dipole-dipole interaction between the resonators. This interaction leads to the formation of the hybridized dimer modes  $\omega_{\pm} = \omega_0 \pm J$ , where the condition  $\omega_L = \omega_R = \omega_0$  corresponds to perfect hybridization. Consequently, the coupling  $\kappa$  of the left resonator to the microwave environment is shared between the dimer modes; in the case of perfect hybridization each inheriting a coupling  $\kappa/2$  (for details see Appendix C). When a pump tone is applied between the hybridized modes, 4-wave mixing converts two pump photons into one signal and one idler photon, split between the modes of the dimer. This implements a phase-preserving amplifier with signal-pump detuning  $J$ .

While Eq. (1) has the necessary ingredients for parametric amplification, in order to achieve a practically useful device, two main constraints on the system parameters need to be fulfilled. Firstly, the Kerr coefficients  $K_i/2\pi$  should be in the 1-100 kHz range, which can be challenging to engineer in devices using disordered superconductors [35], but is easily reachable in our case thanks to the low critical current density in grAl. By using a grAl strip  $0.2 \mu\text{m}$  wide and  $7 \mu\text{m}$  long, we obtain  $K_i/2\pi = 2 \pm 1 \text{ kHz}$  (see Appendix D). Secondly, in order for both modes to be efficiently driven by the same pump, the coupling strength should satisfy the condition  $J \lesssim 2\kappa$ , discussed in detail in Ref. [52]. At the same time, in order to maximize the gain-bandwidth product, we aim to increase  $\kappa$  as much as possible. We design the grAlPA to have  $J/2\pi = 0.1 \text{ GHz}$  and  $\kappa/2\pi = 60 \text{ MHz}$ .

When placed under in-plane magnetic field, the dimer shifts down in frequency as shown in the upper panel of Fig. 1(e), tuning by approximately 300 MHz at  $B_{\parallel} = 1$  T, without suffering from added losses (see Appendix E). This shift is explained by an increase of the grAl kinetic inductance, corresponding to a suppression of the superconducting gap when approaching its critical magnetic field (cf. Refs. [42–44] and Appendix F). The relatively wide capacitive pads of the grAlPA expose them to residual out-of-plane magnetic field components, which can lead to trapped vortices and correspondingly increased dissipation. To avoid this issue and align the field direction to within 1% in-plane, we use a custom-designed 2D vector magnet and we follow a similar procedure as described in Ref. [42] (see Appendix G). Importantly, as illustrated in the lower panel of Fig. 1(e), the hopping strength  $J$  changes by less than 10% over the entire field range, preserving the conditions for parametric amplification up to 1 Tesla.

Figure 2(a) shows the gain performance of the grAlPA in zero magnetic field, as a function of increasing pump power at fixed frequency. We define the gain of the amplifier as the ratio between the reflected power with the pump on and off. By increasing the pump power we can obtain a maximum gain  $G_0$  of 30 dB before entering the multistable regime (see Appendix H). We extract the instantaneous bandwidth (BW) for each gain profile using a Lorentzian fit and we obtain a constant gain-bandwidth product  $\sqrt{G_0} \cdot \text{BW} = (\kappa/2)/2\pi = 22.5$  MHz, as illustrated in the right hand panel of Fig. 2(a). Conveniently, the signal-pump detuning is in the 0.1 GHz range, as expected from the design value for the hopping term  $J$ , facilitating pump tone filtering at the output of the grAlPA. The frequency shift of the gain curves with increasing pump power is due to the AC stark shift of the dimer modes. Another practical aspect of the amplifier is that its gain profiles can be tuned by up to 50 MHz by adjusting the pump frequency (see Appendix H).

The dynamic range of the grAlPA is quantified by the so-called 1-dB compression point, defined as the input signal-probe power for which the maximum gain  $G_0$  decreases by 1 dB. For this purpose, we first calibrate the attenuation of the input line using the resonance fluorescence of a frequency-tunable transmon qubit [54, 55]. The qubit is measured in a separate experiment using the same connections and sample holder utilized for the grAlPA. The main advantage of this method, compared to using a calibrated noise source at the amplifier input, is that it removes the ambiguity of possible insertion losses between the source and the amplifier. By flux-tuning the frequency of the qubit we calibrate the line attenuation in a 1.5 GHz frequency range (see Appendix I). Using this calibration, in Figure 2(b) we present the measured 1-dB compression points for  $G_0 = 20$  dB. We obtain values of  $-111 \pm 2$  dBm for both modes, on par with state-of-the-art implementations using arrays of Josephson junctions [50, 56–58] and sufficient to perform readout with signal powers corresponding to hundreds of circulating photons.

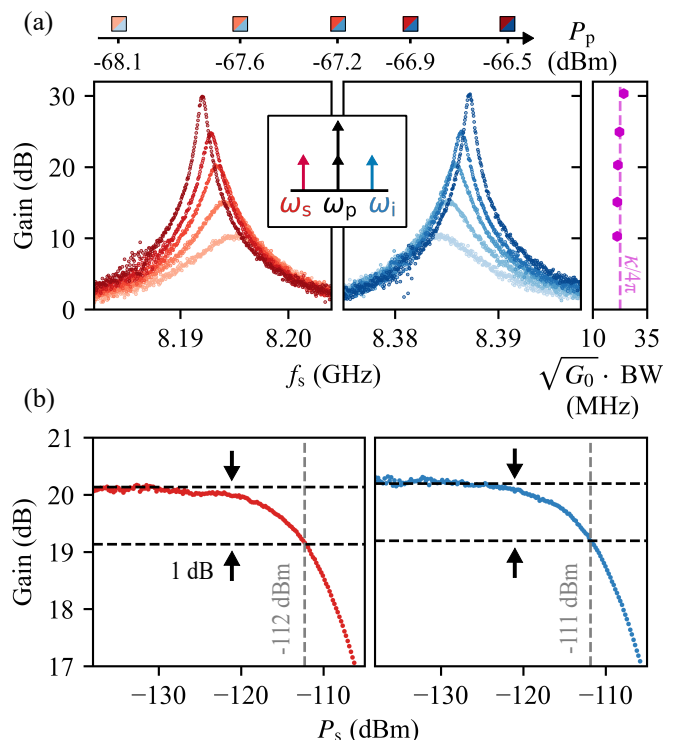


**Figure 2. Gain performance in zero field.** (a) Gain profiles of the grAlPA as a function of signal frequency  $f_s$ , for different pump powers  $P_p$ . The inset shows a schematic of the four wave mixing process giving rise to phase preserving amplification: two photons from a strong pump applied at a frequency between the modes of the dimer (black arrows) are converted into a signal photon (red arrow) and an idler photon (blue arrow), each populating one of the modes of the dimer. The detuning between the pump frequency  $f_p = 8.29$  GHz (not shown in the figure) and the regions of gain is  $\sim 0.1$  GHz. The right hand panel shows the measured gain-bandwidth trade-off characteristic for standing wave amplifiers, following the relation  $\sqrt{G_0} \cdot \text{BW} = (\kappa/2)/2\pi = 22.5$  MHz. (b) Saturation power measurements for the two modes of the grAlPA.  $P_s$  is the signal power at the input of the grAlPA. The 1-dB compression point is indicated by the lower horizontal dashed line and the grey labels indicate the corresponding input power.

In Fig. 3(a) we demonstrate that the grAlPA can be successfully operated at  $G_0 = 20$  dB gain in magnetic fields up to 1 Tesla. Due to the field dependence of the dimer frequency, at each field bias the frequency of the pump needs to be adjusted, as indicated by the arrows in Fig. 3(a). Thanks to the fact that  $K$  and  $J$  are changing less than 10% in field, the pump power is approximately independent on magnetic field ( $\approx -67$  dBm). Using a Lorentzian fit, we quantify the product  $\sqrt{G_0} \cdot \text{BW}$  and we observe a 30% decrease from zero field to 1 T, consistent with the measured change in  $\kappa$ , as illustrated in the right panel of Fig. 3(a). The progressive decoupling of the dimer in magnetic field is explained by the frequency shift of the modes away from the cylindrical waveguide cutoff (see Appendix F). In Fig. 3(b) and (c) we present

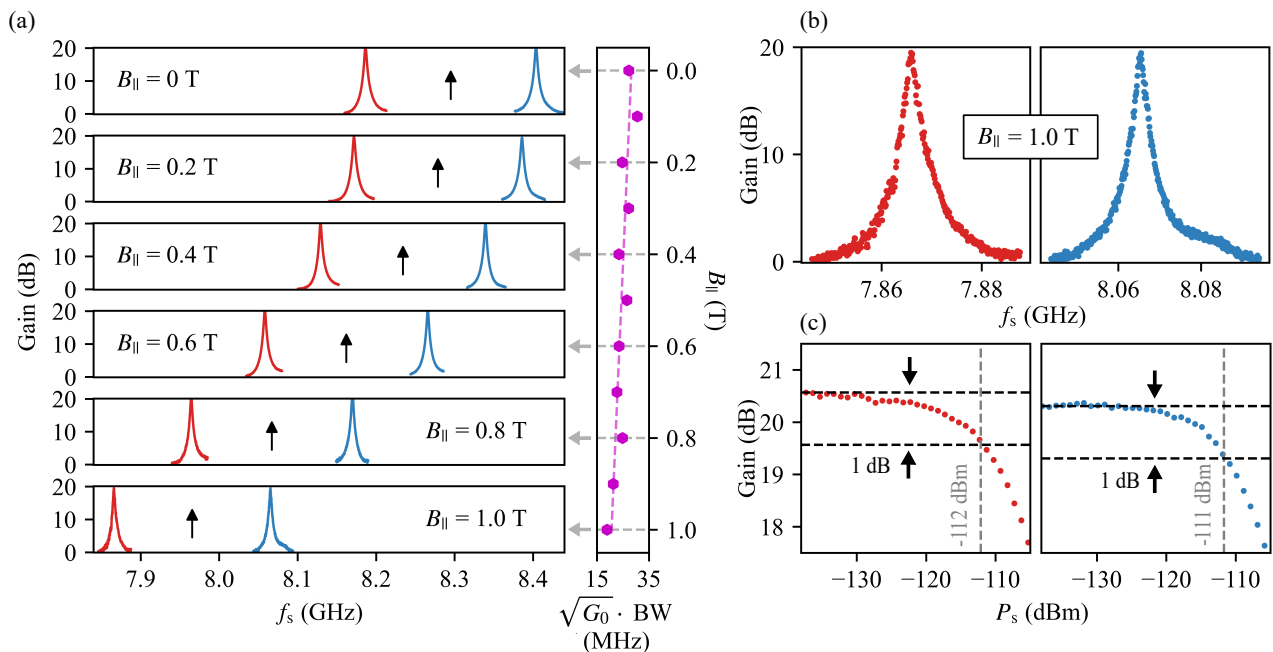


**Figure 3. Gain performance resilient to in-plane magnetic field.** (a) The six left panels show measured gain profiles at magnetic fields  $B_{||} = 0, 0.2, 0.4, 0.8,$  and  $1.0$  T, applied in parallel to the grAl film. The black arrows indicate the frequency of the pump. Note that  $G_0 = 20$  dB can be achieved at any field up to 1 T. The right panel depicts the gain-bandwidth product vs  $B_{||}$ , extracted from Lorentzian fits of measured gain profiles with  $G_0 = 20$  dB. The trend of decreasing  $\sqrt{G_0} \cdot \text{BW}$  is explained by the gradual decoupling of the dimer as the frequencies of the modes move away from the cylindrical waveguide cut-off at  $\approx 60$  GHz (see Appendix F). The dashed purple line illustrates the  $\kappa/2$  values measured from the resonant response of the dimer frequencies while having the pump off. (b) Measured gain of the grAIPA at  $B_{||} = 1$  T. The shoulder visible in the lineshape of the high frequency mode (blue) arises from the normalisation of the gain curve with respect to the pump-off response, which shows a -1 dB dip on resonance (see Appendix J). (c) Saturation power measurements for the two modes of the grAIPA at  $B_{||} = 1$  T. The 1-dB compression point is indicated by the lower horizontal dashed line and the grey labels indicate the corresponding input power. Note that the saturation power at 1 T is not degraded compared to zero field.

measured gain profiles at 20 dB and their corresponding power saturation for  $B_{||} = 1$  T. We find it remarkable that the grAIPA performance at  $B_{||} = 1$  T is comparable to that at  $B_{||} = 0$  T. The shoulder visible in the lineshape of the high frequency mode is explained by a 1 dB dip in the background signal measured without the pump, due to internal losses in the grAl resonators (see Appendix J).

Arguably the most important figure of merit of parametric amplifiers is the improvement they provide to the signal-to-noise (SNR) of a readout chain. In Fig 4(a), we illustrate the near-quantum limited noise performance of the grAIPA at 0 T. We measure the power spectral density (PSD) of the output line connected to the grAIPA, when the pump tone is on and off. To convert the PSD into a temperature scale, we use a pilot tone at  $f_s = 8.193$  GHz, calibrated using the resonance fluorescence of our qubit (see Appendix I). When the pump is off, the noise floor is dominated by a High Electron Mobility Transistor (HEMT) amplifier showing a noise temperature of about 4 K, close to its 3 K nominal value [59]. By operating the grAIPA at 20 dB gain we obtain 10 dB of SNR improvement ( $\Delta\text{SNR}$ ), which corresponds to an input-referred noise approaching the standard quantum limit for phase preserving amplifiers [60].

This result is confirmed in a separate experiment, where the transmon qubit is directly connected at the input of the grAIPA and the pilot tone is calibrated in-situ (see Appendices K and L). We define the operational region of the amplifier as the set of pump powers and frequencies that provide stable  $\Delta\text{SNR} \geq 10$  dB, as illustrated in 4(b).

The grAIPA noise performance under in-plane magnetic field up to  $B_{||} = 1$  T is shown in Fig. 4(c). We report the input referred noise  $n_{\text{in}}$  in units of photons, calculated using the relation  $n_{\text{in}} = k_B \bar{T}_{\text{in}} / hf_s$ , where  $\bar{T}_{\text{in}}$  is the noise temperature floor extracted from the PSD with the grAIPA on. The quantum limit is given by  $n_{\text{in}} = 1$ , with half a photon coming from vacuum fluctuations and half a photon of added noise from the amplifier. Remarkably, the grAIPA remains near quantum-limited up to  $B_{||} = 1$  T, illustrating its utility for quantum readout in magnetic field. We attribute the upturn visible in the grAIPA noise above 0.6 T to spurious vortices in the capacitor pads, which can create additional loss channels [61, 62] and should be suppressed in future designs.

In summary, we have demonstrated a parametric amplifier, nicknamed grAIPA, which relies exclusively on granular aluminum for its nonlinearity. Using the equiv-

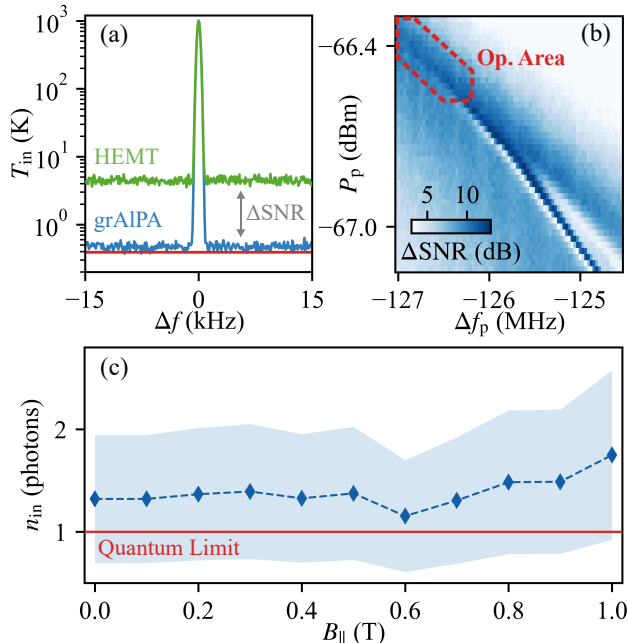


Figure 4. **Noise performance of the grAIPA.** (a) Input-referred noise temperature at  $B_{||} = 0$  T as a function of the detuning  $\Delta f$  from a power-calibrated tone at  $f_s = 8.193$  GHz (see Appendix I for the details on the power calibration). The green and blue solid lines represent measurements with the grAIPA pump off and on, respectively. When the grAIPA is on, the noise approaches the standard quantum limit for non-degenerate amplification indicated by the solid red line. The signal-to-noise improvement ( $\Delta\text{SNR}$ ) is defined as the ratio between the baselines of the green and blue curves. (b)  $\Delta\text{SNR}$  as a function of pump power and signal-pump detuning  $\Delta f_p$  for a fixed coherent tone. The operational area for the grAIPA is defined by the range of parameters where the device is stable and offers  $\Delta\text{SNR}$  larger than 10 dB, as indicated by the dashed contour in red. (c) Input-referred noise as a function of in-plane magnetic field  $B_{||}$ . The quantum limit is defined as the sum of half a photon of noise from vacuum fluctuations and half a photon of added noise from the idler tone of the grAIPA. The blue shaded area indicates the uncertainty propagated from the line-attenuation calibration.

alence between grAl strips and Josephson junction arrays, we have engineered a device similar in performance to state-of-the art Josephson parametric amplifiers, with non-degenerate gain of 20 dB, 28 MHz gain-bandwidth product, 0.1 GHz signal-pump detuning, and saturation power close to -110 dBm. The innate resilience of grAl to in-plane magnetic field enables grAIPAs to operate practically unhindered up to one Tesla and, most importantly, we show that the input-referred noise remains within one added photon above the quantum limit.

Beyond one Tesla, spurious frequency jumps and added losses, likely resulting from residual flux trapping in the pads of the capacitors, hinder the operation of the amplifier. A potential solution is the implementation of artificial pinning sites, similar to the approach described

in Refs. [61, 62]. Furthermore, in order to enable enhanced frequency tunability and increased signal-pump detuning, the grAIPA concept could be expanded to 3-wave mixing by using RF-squids [56, 58, 63–65] made of grAl nanojunctions [44] or by applying a direct current bias [36].

## ACKNOWLEDGEMENTS

We are grateful to Nicolas Roch, Mitchell Field and Mathieu Fechant for fruitful discussions and we acknowledge technical support from S. Diewald, and L. Radtke. Funding was provided by the Deutsche Forschungsgemeinschaft (DFG – German Research Foundation) under project number 450396347 (GeHoldeQED). Funding for the noise calibration was provided by the European Union under the Horizon Europe Program, grant agreement number 101080152 (TruePA). I.T. and T.R. acknowledge support from the German Ministry of Education and Research (BMBF) within the project GEQCOS (FKZ: 13N15683). A.N. acknowledges financing from the Baden-Württemberg Stiftung within the project QT-10 (QEDHiNet). S.G., D.R., and W.W. acknowledge support from the Leibniz award WE 4458-5. Facilities use was supported by the Karlsruhe Nano Micro Facility (KNMF) and KIT Nanostructure Service Laboratory (NSL). We acknowledge qKit for providing a convenient measurement software framework.

## SUPPLEMENTAL MATERIAL

### Appendix A: Inductive participation ratio of grAl nanostrip

The two main inductive contributions in each grAl resonator arise from the kinetic inductance of the grAl strip  $L_{\text{strip}}$ , which constitutes the source of non-linearity in the grAIPA, and the inductance of the capacitor pads  $L_{\text{pads}}$ , which gives a negligible contribution to non-linearity (cf Fig. 1(b) and (c)). The geometric inductance is two orders of magnitude smaller and we neglect it. To extract an estimation of the sheet inductance  $L_{\square}^k$  of grAl, we use Mattis-Bardeen formula [17]

$$L_{\square}^k = \frac{R_{\square} \hbar}{\pi \Delta} \approx 0.12 \text{ nH}/\square, \quad (\text{A1})$$

where  $R_{\square} = \rho/t$  is the sheet resistance and  $\rho$  the resistivity of the grAl film,  $t$  is the thickness of the film and  $\Delta$  is its superconducting gap estimated from Ref. [66]. The grAl strip accounts for 35 squares of sheet inductance, which gives  $L_{\text{strip}} = 4.20$  nH. Using finite element method (FEM) simulations we obtain  $L_{\text{pads}} \approx 1$  nH. Consequently, the inductance participation ratio of the grAl central line  $p = L_{\text{strip}}/(L_{\text{strip}} + L_{\text{pads}})$  is approximately 80%.

## Appendix B: Fabrication

The grAlPA is fabricated using a single step of electron beam lithography on top of a c-plane sapphire wafer with thickness 330  $\mu\text{m}$ . The substrate is coated with a resist stack of 800 nm MMA EL-13 and 400 nm PMMA A4, followed by an additional 10 nm Au antistatic layer. The grAl resonators are then patterned with a 50 keV e-beam writer and developed using an IPA:H<sub>2</sub>O (3:1) solution at 6°C. Before the metal deposition, the substrate is cleaned with a Ar/O<sub>2</sub> descum process inside a Plassys electron beam evaporator. To improve the vacuum conditions after the initial cleaning step, we use Ti as a getter material. A grAl layer with thickness  $t = 40$  nm and resistivity  $\rho = 830$   $\mu\Omega\text{cm}$  is deposited under zero angle Al evaporation, at 1 nm/s deposition rate and using dynamical oxidation. Finally, the sample is oxidized in-situ for 3 min in a fixed O<sub>2</sub> pressure of 10 mbar, to prevent degradation of the grAl film after exposure to ambient conditions. The Nb coupling pad visible in Fig. 1(b) is fabricated in a subsequent optical lithography step using a mask aligner. For the Nb deposition, we use the same substrate cleaning and Ti gettering as for the grAl resonators. We evaporate a 40 nm Nb film at a deposition rate of about 1.2 nm/s.

## Appendix C: Engineering the hybridization of the grAl resonators

### 1. Hybridization and coupling

We now turn our attention to the impact of the grAl resonator hybridization on the gain performance of the grAlPA. By linearizing the Hamiltonian in Eq. (1), assuming negligible internal losses ( $\kappa_{\pm}$ ) and following the approach of Refs. [49, 52], we derive

$$\omega_{\pm} = \frac{\omega_L + \omega_R}{2} \pm \sqrt{J^2 + \left(\frac{\omega_L - \omega_R}{2}\right)^2} \quad (\text{C1})$$

and

$$\kappa_{\pm} = \frac{\kappa}{2} \left( 1 \pm \frac{\omega_L - \omega_R}{\sqrt{4J^2 + (\omega_L - \omega_R)^2}} \right), \quad (\text{C2})$$

where  $\kappa_{\pm}$  are the linewidths of the dimer modes. The scaling of the grAlPA instantaneous bandwidth (BW) is given by  $\sqrt{G_0} \cdot \text{BW} = \kappa_{\text{eq}}$ , where  $G_0$  is the maximum gain of the grAlPA and the equivalent linewidth  $\kappa_{\text{eq}}$  is defined as

$$\kappa_{\text{eq}} = \frac{2\kappa_+ \kappa_-}{\kappa_+ + \kappa_-}. \quad (\text{C3})$$

Perfect hybridization,  $\omega_L = \omega_R$ , gives the maximum BW and the total coupling strength  $\kappa$  is equally split between the dimer modes,  $\kappa_+ = \kappa_- = \kappa/2$ . If  $\omega_L \neq \omega_R$ ,

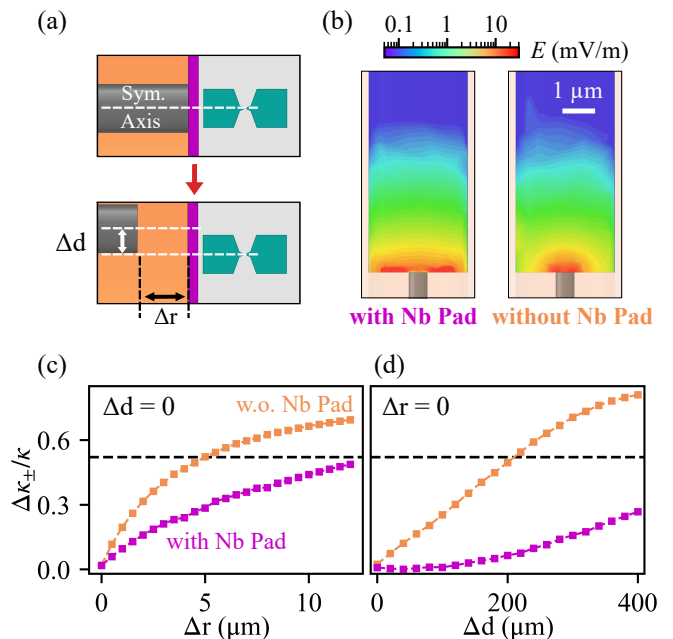


Figure 5. **Finite element simulations of the hybridization susceptibility to misalignments.** (a) Schematic representation of the two cases considered: thermal retraction  $\Delta r$  of the coaxial pin and lateral displacement  $\Delta d$  with respect to the symmetry axis of the waveguide (indicated by the white dashed line). The color code is the same as in Fig. 1(b). (b) Comparison of the electric field distribution across the surface of a sapphire chip with and without the Nb pad. (c), (d) Coupling asymmetry  $\Delta\kappa_{\pm}/\kappa$  as a function of  $\Delta d$  and  $\Delta r$ , respectively. The black dashed line represents an empirical limit above which non-degenerate gain is not achievable (cf. Table I).

besides the reduction of the BW of the amplifier, following Eq. (C2), the linewidths of the dimer modes also show an asymmetry  $\Delta\kappa_{\pm} = |\kappa_+ - \kappa_-|$ . Consequently, we use the asymmetry  $\Delta\kappa_{\pm}$  as a proxy for the hybridization of the resonators.

### 2. The role of the Nb pad

Figure 5 illustrates that the Nb pad reduces the hybridization susceptibility to misalignments. We consider two possible misalignments: lateral displacements ( $\Delta d$ ) due to imperfections of the substrate, and thermal contraction ( $\Delta r$ ) of the coaxial pin during the cooldown (see Fig. 5(a)). In Fig. 5(b) we plot the on-chip distribution of the electric field obtained from finite element simulations in the absence of grAl resonators. We use a driving excitation at 8 GHz and an input power equivalent to a dimer population of 10 photons. We observe that the addition of the Nb pad spreads the electric field lines along the lower edge of the substrate. As a consequence, when using the Nb pads the coupling asymmetry  $\Delta\kappa_{\pm}$  obtained

Table I. Summary of the linear characterization of grALPAs with and without Nb coupling pad. The parameters were extracted from independent cooldowns using the same sample holder. The uncertainty in  $\gamma_{\pm}$  arises from the Fano uncertainty in the measurement setup [51]. We also estimate 10% uncertainty in  $\kappa_{\pm}$  due to the same effect.

Cooldown #	with Nb Pad				without Nb Pad		
	1	2	3	4	1	2	3
$\omega_{+}/2\pi$ (GHz)	8.41	8.38	8.42	8.40	9.35	9.67	9.56
$\omega_{-}/2\pi$ (GHz)	8.21	8.18	8.22	8.22	8.38	8.92	8.90
$\kappa_{+}/2\pi$ (MHz)	23.1	28.2	28.4	26.1	91.9	5.8	85.0
$\kappa_{-}/2\pi$ (MHz)	34.6	38.4	28.11	19.9	15.6	26.11	29.5
$\gamma_{+}/2\pi$ (MHz)	$\leq 5.0$	$\leq 8.0$	$\leq 7.4$	$\leq 6.3$	$\leq 20.6$	$\leq 1.3$	$\leq 21.1$
$\gamma_{-}/2\pi$ (MHz)	$\leq 6.7$	$\leq 10.9$	$\leq 6.8$	$\leq 4.4$	$\leq 2.8$	$\leq 5.4$	$\leq 6.5$
$\omega_{L}/2\pi$ (GHz)	8.29	8.27	8.32	8.33	9.21	9.06	9.39
$\omega_{R}/2\pi$ (GHz)	8.33	8.30	8.32	8.33	8.52	9.53	9.07
$J/2\pi$ (MHz)	99.0	97.0	99.0	90.0	341.0	286.0	286.0
$\kappa/2\pi$ (MHz)	57.7	66.6	56.5	46.0	107.5	31.9	114.5
$\Delta\kappa_{\pm}/\kappa$	0.20	0.15	0.01	0.14	0.71	0.64	0.48
max. $G_0$ (dB)	$\geq 20$	$\geq 20$	$\geq 20$	$\geq 20$	None	None	12

from simulations is less susceptible to misalignments, as shown in Fig. 5(c) and (d).

In Table I we compare two grALPAs fabricated with and without a Nb pad, measured in several successive cooldowns. As expected from simulations, the device with a Nb pad consistently provides gain  $\geq 20$  dB in all four cooldowns, while the sample without a coupling pad only shows non-degenerate gain in one of three cooldowns. For both devices the circuit parameters are extracted from single-tone spectroscopy using Eqs. (C1) and (C2).

#### Appendix D: Kerr coefficients

The non-linearity of our grAl resonators stems from the central grAl strip shown in Fig. 1(c). Following Refs. [41, 52], we estimate the value of the Kerr coefficient  $K$  by modelling the strip as an effective array of  $N_J$  Josephson Junctions (JJ). We consider that the critical current of each junction  $I_c^J$  equals the critical current of the grAl strip  $I_c^{\text{grAl}}$  and provides a Josephson inductance  $L_J = \Phi_0/2\pi I_c^J$ , where  $\Phi_0 = h/2e$  denotes the magnetic flux quantum. The inductance of the grAl strip is  $L_{\text{strip}} = N_J L_J$  and its corresponding self-Kerr coefficient is

$$K = -\frac{E_J}{8\hbar N_J^3} \left( \frac{\omega_r L_{\text{strip}}}{R_Q} \right)^2, \quad (\text{D1})$$

where  $E_J = \Phi_0 I_c^J/2\pi$  is the Josephson energy of the equivalent JJs,  $\omega_r$  the frequency of the resonator and  $R_Q = \hbar/4e^2$  the resistance quantum. We estimate  $I_c^{\text{grAl}}$  from the resistivity of the film, as shown in Ref. [52], while the rest of the parameters are extracted from Table I. For the grAlPA, the JJ array model yields  $K/2\pi = 6\text{--}7$  kHz.

Experimentally, we measure the non-linearity from the power-dependent frequency shifts of the dimer modes. Assuming equal Kerr coefficients for both grAl resonators  $K_L \approx K_R = K$  and applying the rotating-wave approximation, the non-linear part of the grAlPA Hamiltonian can be rewritten as

$$H_{\text{NL}}/\hbar = \sum_{i=+,-} \frac{K}{2} a_i^\dagger a_i a_i^\dagger a_i + \sum_{i<j} \frac{K}{2} a_j^\dagger a_j a_i^\dagger a_i, \quad (\text{D2})$$

where the terms on the right hand side of the equation give the self-Kerr and cross-Kerr frequency shifts, respectively. The mode population  $\bar{n}_{\pm}$  increases linearly with input power  $P_{\text{in}}$ , following

$$\bar{n}_{\pm} = \frac{4P_{\text{in}}}{\hbar\omega_{\pm}} \frac{\kappa_{\pm}}{(\kappa_{\pm} + \gamma_{\pm})^2}, \quad (\text{D3})$$

where  $\omega_{\pm}$  is the resonant frequency of each dimer mode and  $\kappa_{\pm}$ ,  $\gamma_{\pm}$  their external and internal coupling parameters, respectively. The power at the input of the grAlPA ( $P_{\text{in}}$ ) is estimated using the calibration shown in Appendix I. As presented in Fig. 6, all Kerr coefficients of the grAlPA are measured to be in the range of 1-3 kHz and they are unaffected by in-plane magnetic field up to 1 T.

#### Appendix E: Internal losses

Here we report the magnetic field dependence of the internal losses in the grAlPA. We calculate the single-photon internal quality factor  $Q_i$  and external quality factor  $Q_c$  of each dimer mode from circle fits [67] of their respective reflection coefficients at different  $B_{\parallel}$ . As illustrated in Fig. 7(a), both modes preserve  $Q_i/Q_c \gtrsim 10$

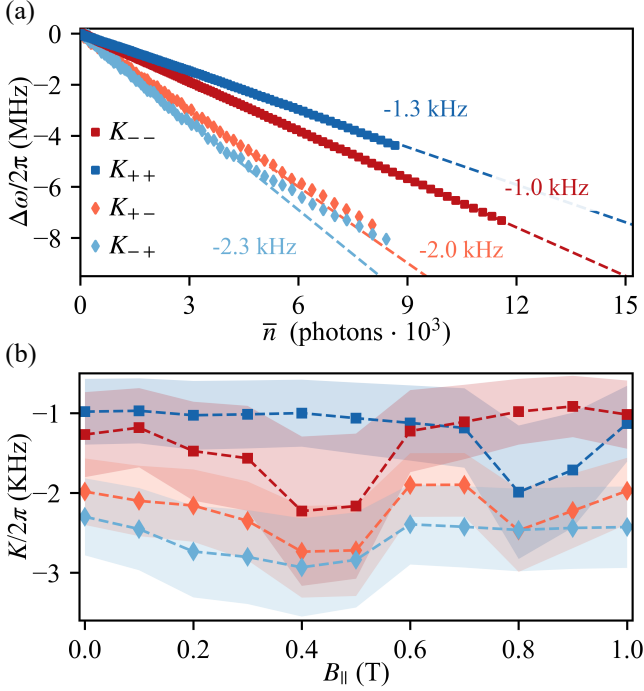


Figure 6. **Self-Kerr and cross-Kerr non-linearities.** (a) Shift in the resonance frequency of each mode of the grAIPA as a function of their average photon number. The shift produced by the self-Kerr ( $K_{++}$  and  $K_{--}$ ) and cross-Kerr ( $K_{+-}$  and  $K_{-+}$ ) non-linearities are measured through single-tone and two-tone spectroscopy, respectively. (b) Magnetic field dependence of the Kerr coefficients. Note that all coefficients remain within the range of 1-3 kHz up to  $B_{||} = 1$  T.

up to  $B_{||} = 1$  T. Due to the strong coupling required for the operation of the amplifier, we can only place a lower bound for the  $Q_i$  value [51]. To extract a more accurate estimation of the internal losses, we would need to decouple the resonators such that they are critically coupled i.e.  $Q_i \approx Q_c$ . In Fig. 7(b) we show the resonant response of one dimer mode for a critically coupled grAIPA, from which we obtain  $Q_i = 9 \cdot 10^4$  with the Fano uncertainty range  $6 \cdot 10^4 < Q_i < 20 \cdot 10^4$ .

#### Appendix F: Magnetic field dependence of the frequency and coupling of the grAl resonators

The frequency of the grAl resonators experiences a shift when we apply an in-plane magnetic field  $B_{||}$ . This effect is produced by the suppression of the superconducting gap  $\Delta$  in field [43],

$$\Delta(B_{||}) = \Delta(0) \sqrt{\frac{1 - (B_{||}/B_c)^2}{1 + (B_{||}/B_c)^2}}, \quad (\text{F1})$$

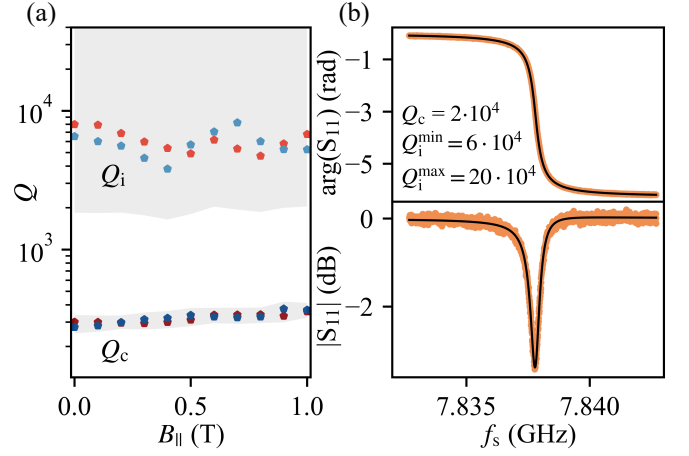


Figure 7. **Internal and external quality factors.** (a) Field dependence of the internal and external quality factors for single-photon population. The size in the error region of  $Q_i$  (upper grey area) comes from the Fano uncertainty of the measurement and the fact that each mode of the grAIPA is overcoupled [51]. Note that  $Q_i$  is at least 2 orders of magnitude above  $Q_c$  for the entire field range. (b) Single-tone spectroscopy of a sample with critical coupling  $Q_i \approx Q_c$ . For this case a reduced Fano uncertainty allows a more accurate estimation of the expected  $Q_i$ . The data in panel (b) is adapted from [52] with permission.

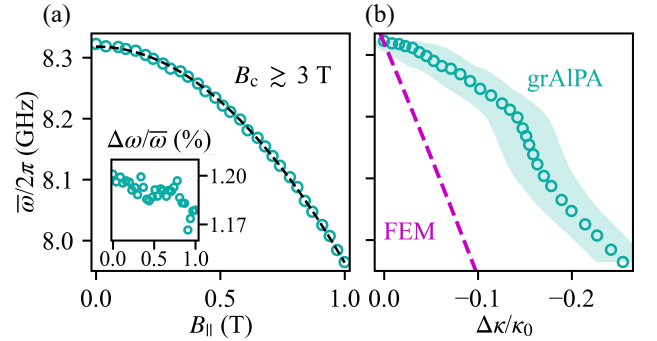


Figure 8. **Magnetic field dependence of  $\bar{\omega}$  and  $\kappa$ .** (a) Field dependence of the average frequency  $\bar{\omega} = (\omega_L + \omega_R)/2$ . The green circles are calculated from single-tone spectroscopy measurements and using Eqs. (C1) and (C2). The dashed black line shows the fit using Eq. (F2), from which we extract a critical field  $B_c \gtrsim 3$  T. The inset displays the relative frequency difference between the modes  $\Delta\omega/\bar{\omega}$ , with  $\Delta\omega = \omega_R - \omega_L$ . (b) Change of the total coupling  $\Delta\kappa$  as a function of  $\bar{\omega}$ . The shaded region represents the Fano uncertainty in the estimation of the external coupling strength  $\kappa$  [51]. The purple dashed line is obtained from finite element simulations. The values of  $\Delta\kappa$  are normalized relative to the coupling  $\kappa_0$  at  $B_{||} = 0$  T.

where  $B_c$  is the in-plane critical field of grAl. From Eq. (A1) we expect an increase of the total kinetic inductance  $L_k$  and a frequency shift following



$$\omega(B_{\parallel}) = \frac{1}{\sqrt{L_{\kappa}(B_{\parallel})C}} = \omega(0) \left( \frac{1 - (B_{\parallel}/B_c)^2}{1 + (B_{\parallel}/B_c)^2} \right)^{1/4}, \quad (\text{F2})$$

where  $C$  is the resonator capacitance. To extract  $B_c$ , we calculate the frequency shift of the grAl resonators from the measured magnetic field dependence of  $\omega_{\pm}$  shown in Fig. 1(d) and using Eqs. (C1) and (C2). As presented in Fig. 8(a), we obtain  $B_c \approx 3$  T. A possible explanation of the fact that  $B_c$  in our experiments is lower than previously reported values of up-to 6 T [42] is the imperfect compensation of out-of-plane magnetic field  $B_{\perp}$  (for details see Appendix G). Lastly, note that the frequencies of the grAl resonators differ by less than 1.5% for all  $B_{\parallel}$  up to 1 T, as shown in the inset of Fig. 8(a).

The decrease of external coupling  $\kappa$  with in-plane field is depicted in Fig. 8(b) and is also visible in the reduction of the instantaneous bandwidth of the grAlPA (see Fig. 2(a)). It arises from the gradual decoupling of the dimer modes as their frequencies move farther from the 60 GHz cutoff of the cylindrical waveguide, as qualitatively confirmed by FEM simulations. We attribute the difference between simulations and measurements of  $\kappa$  to additional features in the environmental impedance seen by the grAlPA, which could be related to the frequency-dependent isolation of the circulators used in our setup [51].

### Appendix G: Magnetic field alignment to minimize the out-of-plane component

The residual out-of-plane magnetic field component  $B_{\perp}$  from misalignment of the substrate inside the cylindrical sample holder in Fig. 1 can lead to trapping of vortices in the grAl resonators [61, 62]. Trapped vortices produce additional loss channels potentially adding noise to the amplifier, especially for  $B_{\parallel}$  approaching 1 T. To mitigate this issue, we calibrate the orientation of the magnetic field following a similar procedure as explained in Ref. [42]. We fix  $B_{\parallel}$  and sweep  $B_{\perp}$  in a range small enough to avoid vortex trapping. Simultaneously, we monitor the phase response in one of the dimer modes at a fixed frequency close to resonance. The phase then follows a quadratic variation with  $B_{\perp}$ , where the maximum indicates the required compensation field.

Note that the field range we can use for the compensation sweep before we trap flux is limited by the width of the capacitor pads [68], which restricts us to a field range almost two orders of magnitude lower compared to Ref. [42]. This limitation is exacerbated by the fact that the modes of the amplifier are strongly coupled, therefore their phase susceptibility to  $B_{\perp}$  is relatively low. To relax this limitation we take advantage of the grAlPA gain-bandwidth product. By applying a pump tone, the linewidths of the dimer modes decrease according to  $\sqrt{G_0} \cdot \text{BW} = \kappa_{\text{eq}}$  (see Eq. (C3)), which for

$G_0 = 18$  dB effectively reduces the linewidth of the dimer modes by a factor of 8 (see Fig. 9(a)). We therefore enhance the sensitivity of the phase to  $B_{\perp}$ , facilitating the measurement of the compensation field. Fig. 9(b) illustrates the result of a compensation sweep at  $B_{\parallel} = 0$  T for the low-frequency dimer mode, with the pump on and off. We observe a clear quadratic trend in the phase only when the pump is on. By repeating the same procedure for different in-plane fields, we obtain the dependence of the compensation field with  $B_{\parallel}$ , which follows a linear trend as depicted in the inset of Fig. 9(b). From the slope of this linear response we extract a misalignment angle of the in-plane magnetic field  $\alpha_{\text{miss}} < 1^{\circ}$ .

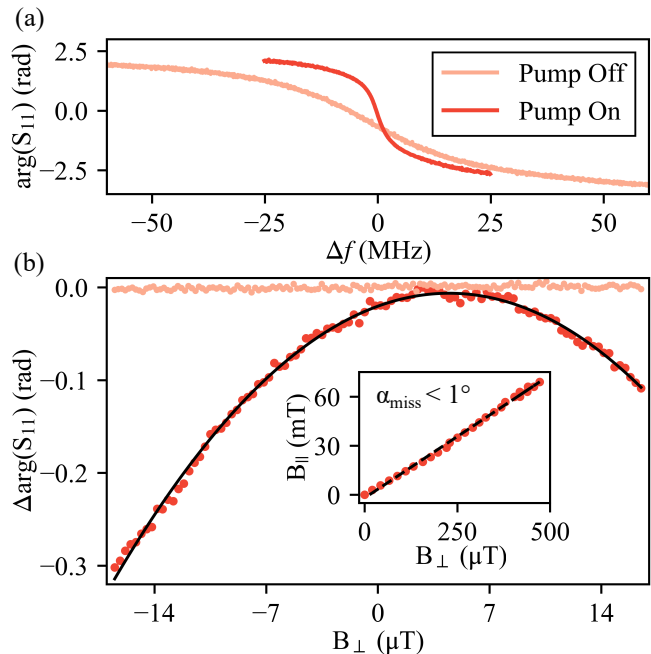


Figure 9. **Compensation of residual out-of-plane magnetic field components.** (a) Phase of the reflection coefficient  $S_{11}$  as a function of the detuning  $\Delta f$  from the resonance frequency  $f_r$ , while having the grAlPA on and off. The narrowing of the response appears as a consequence of the gain-bandwidth trade-off in the grAlPA. We use a pump tone generating a maximum non-degenerate gain of  $G_0 = 18$  dB. This results in a factor of 8 decrease in the linewidth, which improves our detection sensitivity. (b) Example of a compensation sweep employed to calibrate the unwanted  $B_{\perp}$ , while fixing  $B_{\parallel}$  at 0 T. We sweep  $B_{\perp}$  and monitor the change in the phase response  $\Delta \arg(S_{11})$  for a fixed frequency close to  $f_r$ . Note that a non-negligible variation is observed only when the grAlPA pump is on. We determine the compensation field  $B_{\perp}$  by fitting the data with a quadratic function (black solid line) and extracting the field that maximizes  $\Delta \arg(S_{11})$ . The inset displays the compensation fields measured for several values of  $B_{\parallel}$ . The black dashed line depicts a linear fit of the data. The slope of this line provides an estimation of the misalignment angle of the in-plane component, which corresponds to an angle less than  $1^{\circ}$ .

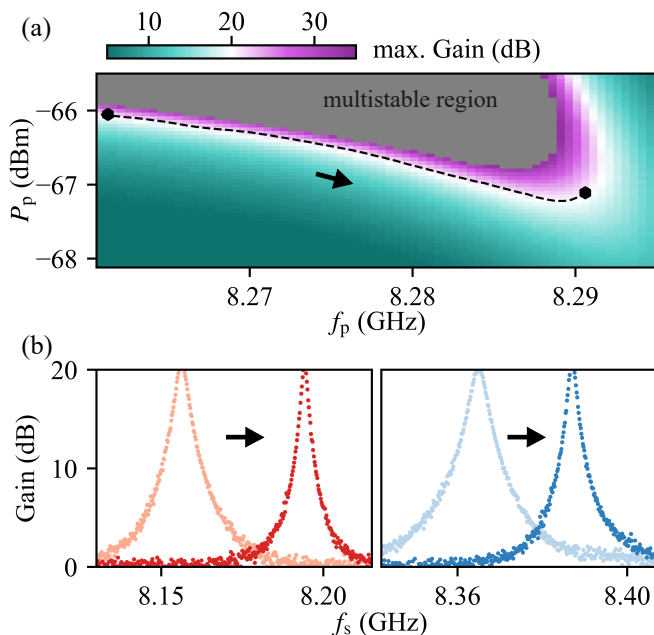


Figure 10. **Frequency tunability of the gain profile.** (a) Maximum gain of grAIPA as a function of the pump frequency and pump power. Regions with 20 dB maximum gain are highlighted by a white fringe, while the grey area represents the multistable regime of the amplifier. The gain profile of the grAIPA is tuned by moving the pump tone along the dashed black line, as shown in (b). We achieve frequency tunability close to 50 MHz for each dimer mode. The narrowing of the Lorentzian gain profiles is attributed to variations in the environmental impedance seen by the grAIPA.

#### Appendix H: Tunability of the gain profile with pump power and frequency

The grAIPA offers additional gain tunability by varying the frequency  $f_p$  and power  $P_p$  of the pump tone. Fig. 10(a) illustrates the dependence of the maximum gain  $G_0$  with  $P_p$  and  $f_p$ . We calculate  $G_0$  by fitting the gain profiles with a Lorentzian function. As marked by the white regions in Fig. 10(a), it is possible to obtain 20 dB gain for various combinations of  $P_p$  and  $f_p$ . Moreover, by increasing the pump power it is possible to increase the gain up to 30 dB, as also depicted in Fig. 10(a). For higher powers the grAIPA enters a multistable regime [49, 52], where parametric amplification is not achievable using our pumping scheme. Note that moving across the 20 dB region, we can tune the gain profile of each dimer mode by approximately  $\approx 50$  MHz, as shown in Fig. 10(b). The change in bandwidth of the gain profiles is attributed to the frequency dependence of the environmental impedance seen by the grAIPA, similar to the effect observed in impedance engineered parametric amplifiers [70].

## Appendix I: Power calibration using the resonant fluorescence of a transmon qubit

### 1. Transmon qubit

To characterize the noise performance in our amplifiers we use the resonant fluorescence produced by the transmon qubit depicted in Fig. 11(a). We use a similar geometry as in Ref [55]. The qubit is designed to fit the cylindrical sample holder used for the grAIPA and consists of a single SQUID junction shunted by a coplanar capacitor with  $C_p = 77$  fF. The capacitor plates are fabricated using a fractal geometry to prevent unwanted flux-trapping while applying an out-of-plane magnetic field. We fabricate the qubit using two steps of optical lithography, followed by zero-angle evaporations of 30 nm and 40 nm pure Al, respectively. Before the evaporation of the second layer, we remove the native oxide layer of the first film employing an Ar milling procedure [71], followed by a static oxidation for 30 min with an oxygen partial pressure of 30 mbar.

The Josephson junctions (JJs) are formed from the overlap of the two Al layers, having an approximate area of  $4 \times 4 \mu\text{m}^2$ . As highlighted in the inset of Figure 11(a), the SQUID loop in our design has an area about  $4 \times 2 \mu\text{m}^2$ . From the geometry of the JJs we expect a junction capacitance  $C_J = 722$  fF and total SQUID capacitance  $C_{SQ} = 2C_J = 1444$  fF. Considering the contribution from the capacitor plates, we expect a total charging energy  $E_C/2\pi = 13$  MHz. We calculate the Josephson energy  $E_J/2\pi$  from the qubit frequency  $f_{ge} = \sqrt{8E_C E_J} - E_C$ , measured using single-tone spectroscopy. We obtain  $E_J/2\pi = 712$  GHz, which confirms that our qubit is in the transmon regime. By increasing the drive power of the qubit we observe the appearance of the second transition frequency  $f_{ef}$ , from which we calculate an anharmonicity of  $\alpha = f_{ef} - f_{ge} = 10$  MHz, consistent with the expected value of  $E_C$  (see Fig. 11(c)). The field dependence of the qubit frequency is presented in Fig. 11(b), which shows that we can operate the qubit within the same frequency range as the grAIPA and use it for power calibration.

### 2. Power calibration

In Fig. 11(d)-(f) we show a typical transmon qubit fluorescence measurement. In the limit of low powers, close to the single-photon regime of the qubit, the shape of reflection coefficient in the quadrature plane approaches a circle, similar to a linear resonator. By increasing the driving power, we observe the characteristic elliptical shape coming from the fluorescence of a two-level system [43, 54, 55]. In the weak drive limit, when the on-resonance Rabi frequency of the qubit satisfies  $\Omega_R \leq \alpha$ , the dependence of  $S_{11}$  with qubit-drive detuning  $\Delta q$  is given by

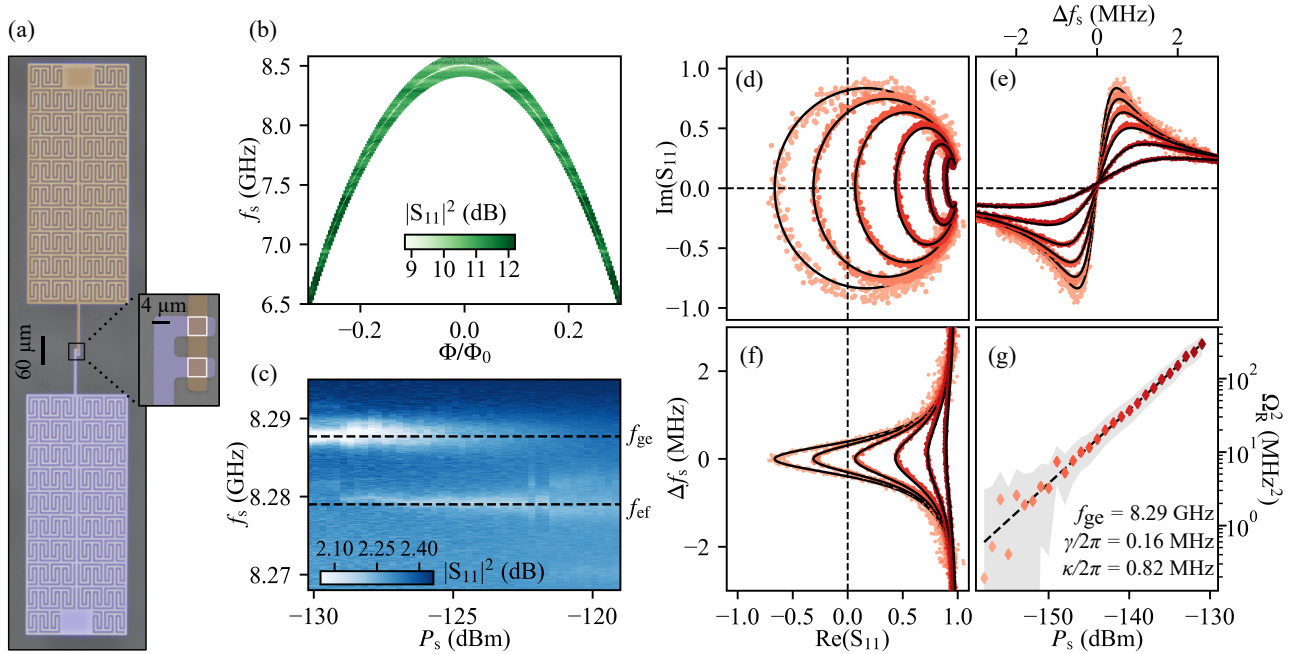


Figure 11. **Resonance fluorescence of a transmon qubit.** (a) False-colored image of the flux tunable transmon qubit used for power calibration. The device is fabricated using 2 steps of optical lithography (brown and purple layers) similar to the implementations shown in [50, 55]. In the inset, we show a magnified image of the squid loop with each Josephson junction highlighted by a white square. (b) Flux dependence of the spectrum of the transmon qubit. The resonance frequency of the qubit appears as a dip of the reflection amplitude  $|S_{11}|$ . (c) Single-tone spectroscopy of the transmon qubit as a function of on-chip power  $P_s$ . From the first ( $f_{ge}$ ) and second transition ( $f_{ef}$ ) frequencies, we extract an anharmonicity  $\alpha \approx 10$  MHz, consistent with the estimated charging energy of the design in (a). (d) Quadrature plane of the reflection coefficient in the vicinity of the qubit frequency at  $f_{ge} = 8.287$  GHz. At low powers the frequency follows a circular shape similar to the response of a linear resonator, from which we extract  $\kappa/2\pi = 828$  KHz and  $\gamma/2\pi = 155$  KHz through a standard circle fit procedure [67]. As power increases, the shape transforms into an ellipse, characteristic of the resonance fluorescence of a two-level system [43, 52, 55, 69]. (e), (f) Real and imaginary part of the reflection coefficient as a function of the detuning from the qubit frequency  $\Delta f_s$ . The black solid lines in panels (d), (e) and (f) are fits of the measurement data using equation (I1). For the fits, we fix the values of  $\kappa$ ,  $\gamma$  and  $f_{ge}$  calculated at the lowest power and use  $\Omega_R$  as the sole fitting parameter. (g) Input power dependence of the Rabi frequency  $\Omega_R$ . The shaded area indicates the Fano uncertainty in  $\kappa$  and  $\gamma$ . We fit the data using equation (I2), from which we extract an input attenuation of  $-89.3 \pm 2$  dB.

$$S_{11} = 1 - \frac{2\kappa}{\Gamma} \frac{1 + 2i\Delta_q/\Gamma}{1 + (2\Delta_q/\Gamma)^2 + 2(\Omega_R/\Gamma)^2}, \quad (\text{I1})$$

$$\Omega_R = A \frac{2\Gamma P_{RT}}{hf_{ge}}, \quad (\text{I2})$$

where  $\Omega_R$  is the on-resonance Rabi frequency of the qubit,  $\kappa$  the external coupling rate,  $\gamma$  the internal loss rate and  $\Gamma = \kappa + \gamma$  the energy relaxation rate. We assume negligible pure dephasing rates  $\Gamma_\phi$ , in comparison to  $\Gamma$ . For each driving power we fit the fluorescence of the transmon qubit using Eq. (I1). The values of  $\kappa/2\pi = 0.82$  MHz and  $\gamma/2\pi = 0.16$  MHz are extracted from the fitting at powers close to the single-photon regime. For higher driving powers, we fix  $\kappa$  and  $\gamma$ , and use  $\Omega_R$  as the only fitting parameter.

We extract the attenuation  $A$  in the input line of our setup by fitting the dependence of  $\Omega_R$  with driving power at room temperature  $P_{RT}$

where the power reaching the input of the transmon qubit is given by  $P_s = A \cdot P_{RT}$ . As presented in Fig. 11(g), we observe a linear dependence between  $P_s$  and  $\Omega_R^2$ , as expected from equation (I2). At 8.287 GHz we calculate an input attenuation of  $-89.3 \pm 2$  dB.

The field tunability of the transmon qubit allows us to perform power calibration in the entire operational range of the grAIIPA, as shown in Fig. 12. The frequency dependence of the attenuation is attributed to the frequency-dependent insertion loss of the coaxial cables. We observe an overall decrease in attenuation of  $\approx 5$  dB from room temperature to 30 mK, which can be explained by the change of resistivity in the coaxial cables.

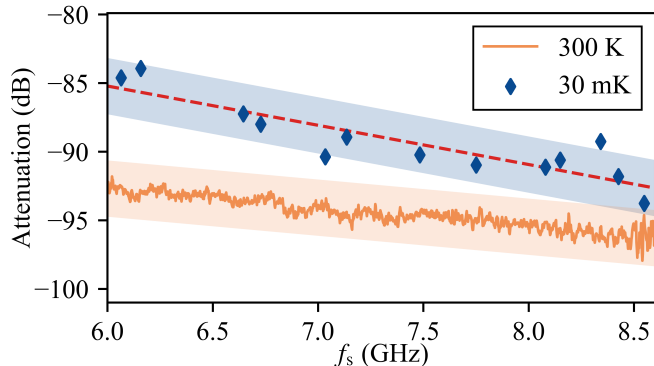


Figure 12. **Input power calibration of the measurement setup.** The scattered data in blue represent the low-temperature attenuation of the input lines (see complete setup in Appendix K). The attenuation is calibrated using the resonance fluorescence of a transmon qubit. The red dashed line denotes the linear fit applied to estimate the low-temperature attenuation used in the characterization of the grAIPA. The error region comes from the uncertainty in the power calibration. For comparison, the orange line shows the attenuation of the input line measured at room temperature. The shaded area indicates the error range.

#### Appendix J: Comparison of the reflection amplitude with and without pump

For our definition of gain, we compare the reflection amplitude  $S_{11}$  of each hybridized mode while having the grAIPA pump on and off. Residual internal losses produce a dip in  $S_{11}$  close to the resonance frequency in the undriven case, giving an apparent asymmetry in the gain

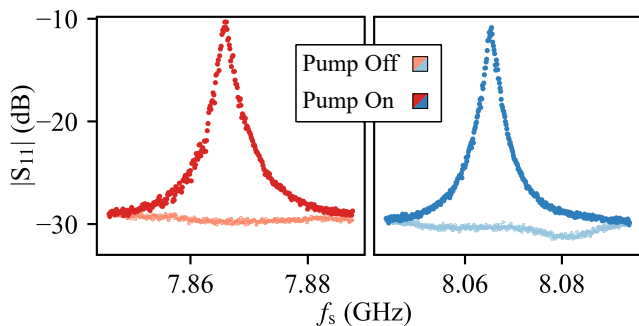


Figure 13. **Reflection amplitude at  $B_{\parallel} = 1$  T.** We compare the amplitude of the reflection coefficient  $S_{11}$  close to each mode of the grAIPA, both with the pump off (light blue and red lines) and on (dark red and blue lines). When driving the grAIPA, the response resembles the expected Lorentzian gain profile. The dip observed at the resonance of the high frequency mode while having the pump off (light blue line on the right panel), explains the additional shoulder seen in the gain profile presented in Fig. 3(b).

profiles. This effect is more evident at  $B_{\parallel} = 1$  T because of the proximity of the gain profiles to the initial resonance of the dimer modes (see Fig. 2(c)). In Fig. 13 we show a comparison of the raw  $S_{11}$  measured in both the driven and undriven case at  $B_{\parallel} = 1$  T. We observe that when the grAIPA pump is on the profile of each mode resembles the expected Lorentzian shape.

#### Appendix K: Measurement setup

We use two different experimental setups, depicted in Fig. 14. For the measurements presented in the main text and in Appendices C-I, we use the configuration shown in Fig. 14(a). The setup is adapted to perform both the input line-attenuation calibration via resonant fluorescence of a transmon qubit (see Appendix I) and the characterization of the grAIPA, using the same sample holder (see Fig. 1(a)) and microwave connections. The response of each device under test (DUT = qubit or grAIPA) is characterized in separate cooldowns using single-port reflection measurements. An input signal generated by a Vector Network Analyzer (VNA) is attenuated by a series of two nominally 30 dB attenuators thermalized to the 4 K and 30 mK plates of our dilution refrigerator, respectively. The remaining microwave components and connections in the input line provide an additional attenuation of about 30 dB. The output signal of the DUT is routed by a cryogenic circulator to a 2-stage isolator and a 12 GHz low-pass filter at the mixing chamber, and then amplified by a HEMT amplifier thermalized at 4 K [59] and a commercial room temperature amplifier. We connect the isolator and the HEMT with a NbTi superconducting cable with negligible insertion loss. We couple the pump tone using a directional coupler at room temperature. The output signal is split by a Wilkinson power divider and directed to the receiving port of the VNA and the input of a spectrum Analyzer (SA). The setup is equipped with a 2D vector magnet thermalized at 4 K, designed to produce in-plane magnetic fields up to 1 T and out-of-plane magnetic fields of the order of 100 mT.

In the second setup configuration, shown in Fig. 14(b), the transmon qubit and the grAIPA are connected and measured in the same cooldown. They are mounted in separate sample holders and placed in different magnetic shields. The pump tone is now coupled at the lowest temperature stage of the dilution refrigerator using a cryogenic directional coupler. We estimate an insertion loss about 1.5 dB between the output of the transmon and the input of the grAIPA. This comes from the circulators (0.4 dB), directional coupler (0.5 dB) and microwave connections (0.6 dB) used in the setup. In this case only the qubit is magnetic field biased using a superconducting coil attached to the sample holder.

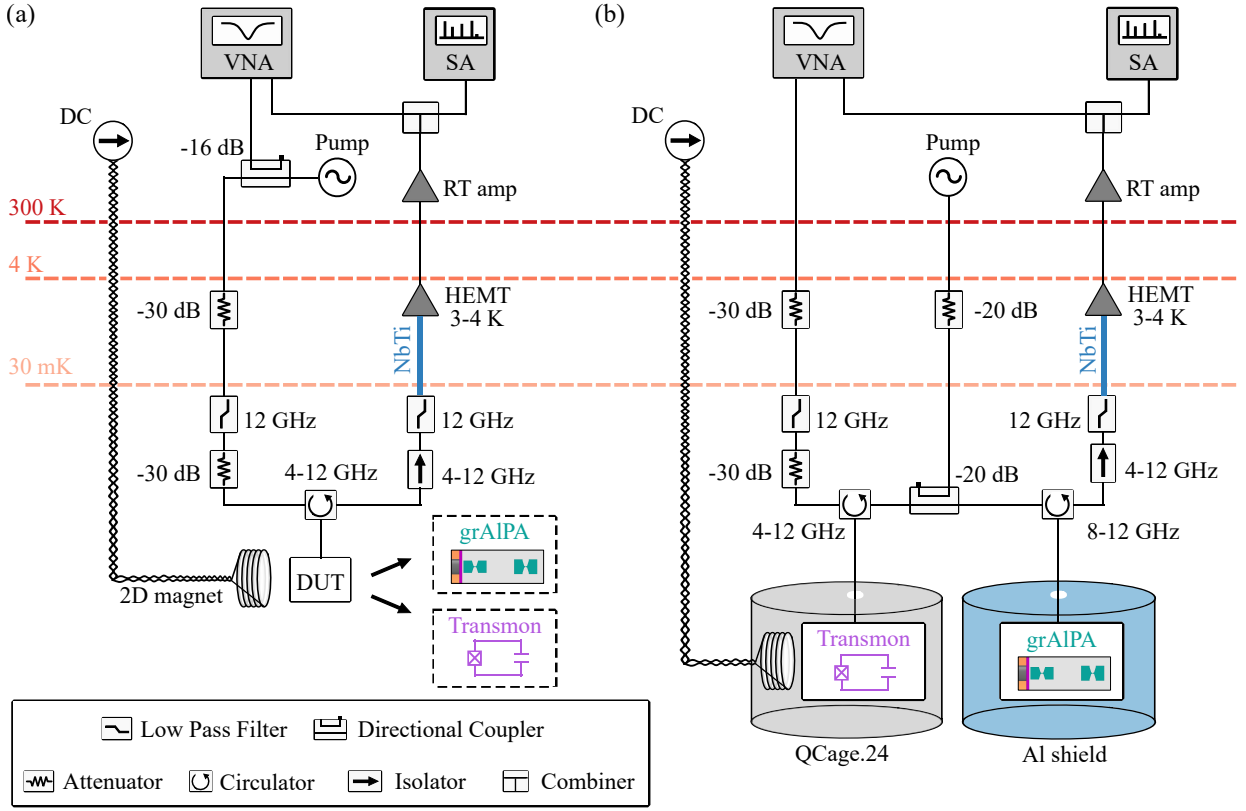


Figure 14. **Experimental setups.** Each component is thermalized to the temperature stage indicated by the nearest dashed line. **(a)** Schematics of the set up employed for the grAIPA measurements presented in the main text. We use the same magnetic-field biasing setup as in Refs. [42, 44, 51]. The magnetic field is generated by a homemade 2D vector magnet, with its orientation calibrated using the method described in Ref. [42] and in Appendix G. To drive the grAIPA, the pump tone is combined through a directional coupler at room temperature with the signal from a vector network analyzer (VNA). A power divider located outside the dilution refrigerator splits the output signal between the receiving port of the VNA and a spectrum analyzer (SA). **(b)** Secondary setup employed for the measurements in Appendix L. The grAIPA is connected via a circulator to a transmon qubit. The transmon qubit is housed inside a QCage.24 magnetic shielding [72] and the grAIPA inside a homemade Al shield. The pump tone is added using a cryogenic directional coupler. In this setup we estimate a total insertion loss between the transmon and the grAIPA on the order of 1.5 dB.

### Appendix L: Noise performance in a secondary experimental setup

In the following, we explain the noise characterization of the grAIPA performed in the secondary setup illustrated in Fig. 14(b). In this case the transmon qubit used for the input power calibration (see Appendix I) is connected before the amplifier in the same cooldown. Figure 15(a) shows the attenuation calculated within the operational range of our amplifier in the absence of magnetic field. Figure 15(b) shows the input referred noise temperature measured using a pilot tone at  $f_s = 8.469$  GHz. When the amplifier is tuned to produce a maximum gain of  $G_0 = 20$  dB, we achieve  $\Delta\text{SNR} \approx 10$  dB and a noise performance approaching the standard quantum limit, in agreement with the results shown in Fig. 4. The increase of the input-referred noise in this experiment, is attributed to the additional inser-

tion loss between the transmon qubit and the grAIPA.

To account for the additional losses between the qubit and the amplifier, we assume that all added components can be modelled as an effective attenuator thermalized to the mixing chamber of the dilution refrigerator ( $T_{\text{Th}} \approx 15$  mK). A schematics is presented in Fig. 15(c). Using a beam-splitter approximation for the effective attenuator, we derive the relation between the noise referred back to the input of the transmon qubit  $T_{\text{in}}$  and the noise added by grAIPA  $T_{\text{gr}}$  as

$$T_{\text{in}} = \frac{T_{\text{out}}}{\lambda G_0 G_{\text{H}}} = T_{\text{s}} + \left( \frac{1-\lambda}{\lambda} \right) T_{\text{Th}} + \frac{T_{\text{gr}}}{\lambda} + \frac{T_{\text{H}}}{\lambda G_0}, \quad (\text{L1})$$

where  $\lambda$  is the insertion loss of the effective attenuator,  $T_{\text{s}}$  the noise accompanying the pilot tone and  $G_{\text{H}}$ ,  $T_{\text{H}}$  the gain and added noise of the HEMT, respectively. Assuming that  $T_{\text{s}} = T_{\text{Th}}$ ,  $T_{\text{gr}}$  is given by vacuum fluctuations (i.e. the grAIPA is quantum limited) and taking  $T_{\text{H}}$  from

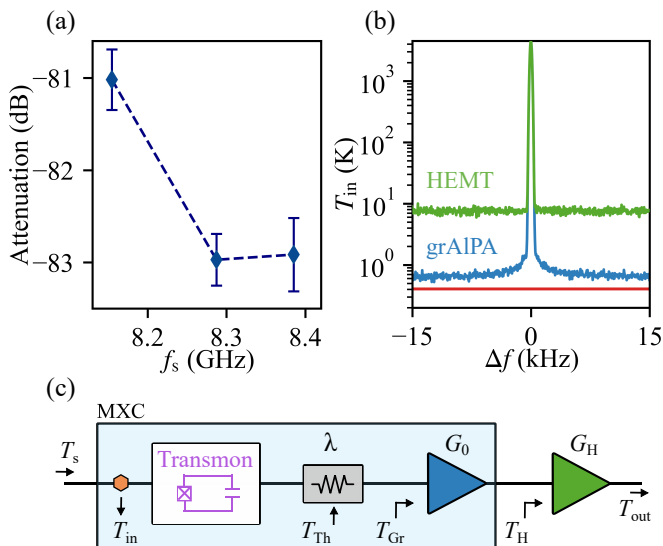


Figure 15. **Noise performance of the grAIPA in the secondary measurement setup.** (a) Input power calibration of the measurement setup shown in Fig. 14(b). The attenuation is calculated using the fluorescence of the transmon qubit explained in Appendix I. (b) Input-referred noise temperature as a function of the detuning  $\Delta f$  from a power-calibrated tone at  $f_s = 8.469$  GHz. The green and blue solid lines represent measurements with the grAIPA pump off and on, respectively. We attribute the increase in input-referred noise compared to Fig. 4(a) to the insertion loss  $\lambda$  between the qubit and the grAIPA. (c) The losses between the qubit and the grAIPA are modeled by an effective attenuator thermalized to the mixing chamber of the dilution refrigerator. The orange marker indicates the point up to which we calibrate the input power.

Fig. 15(b), we obtain  $\lambda \approx 1.8$  dB. This result is consistent with the nominal expected insertion loss of 1.5 dB.

- [1] R. Vijay, D. H. Slichter, and I. Siddiqi, Observation of Quantum Jumps in a Superconducting Artificial Atom, *Phys. Rev. Lett.* **106**, 110502 (2011).
- [2] A. Roy and M. Devoret, Introduction to parametric amplification of quantum signals with Josephson circuits, *C. R. Phys.* **17**, 740 (2016).
- [3] J. Aumentado, Superconducting Parametric Amplifiers: The State of the Art in Josephson Parametric Amplifiers, *IEEE Microwave Mag.* **21**, 45 (2020).
- [4] M. Esposito, A. Ranadive, L. Planat, and N. Roch, Perspective on traveling wave microwave parametric amplifiers, *Appl. Phys. Lett.* **119** (2021).
- [5] S. Krinner, N. Lacroix, A. Remm, A. Di Paolo, E. Genois, C. Leroux, C. Hellings, S. Lazar, F. Swiadek, J. Herrmann, G. J. Norris, C. K. Andersen, M. Müller, A. Blais, C. Eichler, and A. Wallraff, Realizing repeated quantum error correction in a distance-three surface code, *Nature* **605**, 669 (2022).
- [6] T. White, Readout of a quantum processor with high dynamic range Josephson parametric amplifiers, *Appl. Phys. Lett.* **122** (2023).
- [7] Google Quantum AI, Suppressing quantum errors by scaling a surface code logical qubit, *Nature* **614**, 676 (2023).
- [8] V. V. Sivak, A. Eickbusch, B. Royer, S. Singh, I. Tsioutsios, S. Ganjam, A. Miano, B. L. Brock, A. Z. Ding, L. Frunzio, S. M. Girvin, R. J. Schoelkopf, and M. H. Devoret, Real-time quantum error correction beyond break-even, *Nature* **616**, 50 (2023).
- [9] V. Vesterinen, O.-P. Saira, I. Räisänen, M. Möttönen, L. Grönberg, J. Pekola, and J. Hassel, Lumped-element Josephson parametric amplifier at 650 MHz for nanocalorimeter readout, *Supercond. Sci. Technol.* **30**, 085001 (2017).
- [10] Z. K. Mineev, S. O. Mundhada, S. Shankar, P. Reinhold, R. Gutiérrez-Jáuregui, R. J. Schoelkopf, M. Mirrahimi, H. J. Carmichael, and M. H. Devoret, To catch and reverse a quantum jump mid-flight, *Nature* **570**, 200 (2019).
- [11] R. Kokkonen, J. Govenius, V. Vesterinen, R. E. Lake, A. M. Gunyhó, K. Y. Tan, S. Simbierowicz, L. Grönberg, J. Lehtinen, M. Prunnila, J. Hassel, A. Lamminen, O.-P. Saira, and M. Möttönen, Nanobolometer with ultralow noise equivalent power, *Commun. Phys.* **2**, 1 (2019).

- [12] Z. Wang, L. Balembois, M. Rančić, E. Billaud, M. Le Dantec, A. Ferrier, P. Goldner, S. Bertaina, T. Chanelière, D. Esteve, D. Vion, P. Bertet, and E. Flurin, Single-electron spin resonance detection by microwave photon counting, *Nature* **619**, 276 (2023).
- [13] R. Assouly, R. Dassonneville, T. Peronnin, A. Bienfait, and B. Huard, Quantum advantage in microwave quantum radar, *Nat. Phys.* **19**, 1418 (2023).
- [14] K. W. Murch, S. J. Weber, C. Macklin, and I. Siddiqi, Observing single quantum trajectories of a superconducting quantum bit, *Nature* **502**, 211 (2013).
- [15] K. Serniak, S. Diamond, M. Hays, V. Fatemi, S. Shankar, L. Frunzio, R. J. Schoelkopf, and M. H. Devoret, Direct Dispersive Monitoring of Charge Parity in Offset-Charge-Sensitive Transmons, *Phys. Rev. Appl.* **12**, 014052 (2019).
- [16] M. Spiecker, P. Paluch, N. Gosling, N. Drucker, S. Matityahu, D. Gusenkova, S. Günzler, D. Rieger, I. Takmakov, F. Valenti, P. Winkel, R. Gebauer, O. Sander, G. Catelani, A. Shnirman, A. V. Ustinov, W. Wernsdorfer, Y. Cohen, and I. M. Pop, Two-level system hyperpolarization using a quantum Szilard engine, *Nat. Phys.* **19**, 1320 (2023).
- [17] M. Tinkham, *Introduction to Superconductivity* (2004).
- [18] A. Schneider, T. Wolz, M. Pfirrmann, M. Spiecker, H. Rotzinger, A. V. Ustinov, and M. Weides, Transmon qubit in a magnetic field: Evolution of coherence and transition frequency, *Phys. Rev. Res.* **1**, 023003 (2019).
- [19] J. Krause, C. Dickel, E. Vaal, M. Vielmetter, J. Feng, R. Bounds, G. Catelani, J. M. Fink, and Y. Ando, Magnetic Field Resilience of Three-Dimensional Transmons with Thin-Film Al/AIO<sub>x</sub>/Al Josephson Junctions Approaching 1 T, *Phys. Rev. Appl.* **17**, 034032 (2022).
- [20] S. Schaal, I. Ahmed, J. A. Haigh, L. Hutin, B. Bertrand, S. Barraud, M. Vinet, C.-M. Lee, N. Stelmashenko, J. W. A. Robinson, J. Y. Qiu, S. Hacoheh-Gourgy, I. Siddiqi, M. F. Gonzalez-Zalba, and J. J. L. Morton, Fast Gate-Based Readout of Silicon Quantum Dots Using Josephson Parametric Amplification, *Phys. Rev. Lett.* **124**, 067701 (2020).
- [21] V. Elhomsy, L. Planat, D. J. Niegemann, B. Cardoso-Paz, A. Badreldin, B. Klemt, V. Thiney, R. Lethiecq, E. Eyraud, M. C. Dartiaill, B. Bertrand, H. Niebojewski, C. Bäuerle, M. Vinet, T. Meunier, N. Roch, and M. Urdampilleta, Broadband parametric amplification for multiplexed SiMOS quantum dot signals, *arXiv* (2023), 2307.14717.
- [22] M. Pita-Vidal, A. Bargerbos, R. Žitko, L. J. Splitthoff, L. Grünhaupt, J. J. Wesdorp, Y. Liu, L. P. Kouwenhoven, R. Aguado, B. van Heck, A. Kou, and C. K. Andersen, Direct manipulation of a superconducting spin qubit strongly coupled to a transmon qubit, *Nat. Phys.* **19**, 1110 (2023).
- [23] M. Hays, V. Fatemi, D. Bouman, J. Cerrillo, S. Diamond, K. Serniak, T. Connolly, P. Krogstrup, J. Nygård, A. L. Yeyati, A. Geresdi, and M. H. Devoret, Coherent manipulation of an Andreev spin qubit, *Science* **373**, 430 (2021).
- [24] A. Bienfait, J. J. Pla, Y. Kubo, M. Stern, X. Zhou, C. C. Lo, C. D. Weis, T. Schenkel, M. L. W. Thewalt, D. Vion, D. Esteve, B. Julsgaard, K. Mølmer, J. J. L. Morton, and P. Bertet, Reaching the quantum limit of sensitivity in electron spin resonance, *Nat. Nanotechnol.* **11**, 253 (2016).
- [25] W. Vine, M. Savytskyi, A. Vaartjes, A. Kringhøj, D. Parker, J. Slack-Smith, T. Schenkel, K. Mølmer, J. C. McCallum, B. C. Johnson, A. Morello, and J. J. Pla, In situ amplification of spin echoes within a kinetic inductance parametric amplifier, *Sci. Adv.* **9** (2023).
- [26] C. Godfrin, A. Ferhat, R. Ballou, S. Klyatskaya, M. Ruben, W. Wernsdorfer, and F. Balestro, Operating Quantum States in Single Magnetic Molecules: Implementation of Grover's Quantum Algorithm, *Phys. Rev. Lett.* **119**, 187702 (2017).
- [27] S. K. Lamoreaux, K. A. van Bibber, K. W. Lehnert, and G. Carosi, Analysis of single-photon and linear amplifier detectors for microwave cavity dark matter axion searches, *Phys. Rev. D* **88**, 035020 (2013).
- [28] K. M. Backes, D. A. Palken, S. A. Kenany, B. M. Brubaker, S. B. Cahn, A. Droster, G. C. Hilton, S. Ghosh, H. Jackson, S. K. Lamoreaux, A. F. Leder, K. W. Lehnert, S. M. Lewis, M. Malnou, R. H. Maruyama, N. M. Rapidis, M. Simanovskaia, S. Singh, D. H. Speller, I. Urdinaran, L. R. Vale, E. C. van Assendelft, K. van Bibber, and H. Wang, A quantum enhanced search for dark matter axions, *Nature* **590**, 238 (2021).
- [29] C. Braggio, G. Cappelli, G. Carugno, N. Crescini, R. Di Vora, M. Esposito, A. Ortolan, L. Planat, A. Ranadive, N. Roch, and G. Ruoso, A haloscope amplification chain based on a traveling wave parametric amplifier, *Rev. Sci. Instrum.* **93** (2022).
- [30] L. M. Janssen, G. Butseraen, J. Krause, A. Coissard, L. Planat, N. Roch, G. Catelani, Y. Ando, and C. Dickel, Magnetic-field dependence of a Josephson traveling-wave parametric amplifier and integration into a high-field setup, *arXiv* (2024), 2402.19398.
- [31] J. Sarkar, K. V. Salunkhe, S. Mandal, S. Ghatak, A. H. Marchawala, I. Das, K. Watanabe, T. Taniguchi, R. Vijay, and M. M. Deshmukh, Quantum-noise-limited microwave amplification using a graphene Josephson junction, *Nat. Nanotechnol.* **17**, 1147 (2022).
- [32] G. Butseraen, A. Ranadive, N. Aparicio, K. Rafsanjani Amin, A. Juyal, M. Esposito, K. Watanabe, T. Taniguchi, N. Roch, F. Lefloch, and J. Renard, A gate-tunable graphene Josephson parametric amplifier, *Nat. Nanotechnol.* **17**, 1153 (2022).
- [33] D. Phan, P. Falthansl-Scheinecker, U. Mishra, W. M. Strickland, D. Langone, J. Shabani, and A. P. Higginbotham, Gate-Tunable Superconductor-Semiconductor Parametric Amplifier, *Phys. Rev. Appl.* **19**, 064032 (2023).
- [34] L. J. Splitthoff, J. J. Wesdorp, M. Pita-Vidal, A. Bargerbos, Y. Liu, and C. K. Andersen, Gate-tunable kinetic inductance parametric amplifier, *Phys. Rev. Appl.* **21**, 014052 (2024).
- [35] M. Xu, R. Cheng, Y. Wu, G. Liu, and H. X. Tang, Magnetic Field-Resilient Quantum-Limited Parametric Amplifier, *PRX Quantum* **4**, 010322 (2023).
- [36] S. Frasca, C. Roy, G. Beaulieu, and P. Scarlino, Three-wave-mixing quantum-limited kinetic inductance parametric amplifier operating at 6 T near 1 K, *Phys. Rev. Appl.* **21**, 024011 (2024).
- [37] M. Khalifa and J. Salfi, Nonlinearity and Parametric Amplification of Superconducting Nanowire Resonators in Magnetic Field, *Phys. Rev. Appl.* **19**, 034024 (2023).
- [38] D. J. Parker, M. Savytskyi, W. Vine, A. Laucht, T. Duty, A. Morello, A. L. Grimsmo, and J. J. Pla, Degenerate

- Parametric Amplification via Three-Wave Mixing Using Kinetic Inductance, *Phys. Rev. Appl.* **17**, 034064 (2022).
- [39] A. Vaartjes, A. Kringhøj, W. Vine, T. Day, A. Morello, and J. J. Pla, Strong Microwave Squeezing Above 1 Tesla and 1 Kelvin, *arXiv* (2023), 2311.07968.
- [40] A. Mohamed, E. Zohari, J. J. Pla, P. E. Barclay, and S. Barzanjeh, Selective Single and Double-Mode Quantum Limited Amplifier, *arXiv* (2023), 2311.11496.
- [41] N. Maleeva, L. Grünhaupt, T. Klein, F. Levy-Bertrand, O. Dupre, M. Calvo, F. Valenti, P. Winkel, F. Friedrich, W. Wernsdorfer, A. V. Ustinov, H. Rotzinger, A. Monfardini, M. V. Fistul, and I. M. Pop, Circuit quantum electrodynamics of granular aluminum resonators, *Nature Communications* **9**, 3889 (2018).
- [42] K. Borisov, D. Rieger, P. Winkel, F. Henriques, F. Valenti, A. Ionita, M. Wessbecher, M. Spiecker, D. Gusenkova, I. M. Pop, and W. Wernsdorfer, Superconducting granular aluminum resonators resilient to magnetic fields up to 1 tesla, *Applied Physics Letters* **117** (2020).
- [43] P. Winkel, K. Borisov, L. Grünhaupt, D. Rieger, M. Spiecker, F. Valenti, A. V. Ustinov, W. Wernsdorfer, and I. M. Pop, Implementation of a Transmon Qubit Using Superconducting Granular Aluminum, *Phys. Rev. X* **10**, 031032 (2020).
- [44] D. Rieger, S. Günzler, M. Spiecker, P. Paluch, P. Winkel, L. Hahn, J. K. Hohmann, A. Bacher, W. Wernsdorfer, and I. M. Pop, Granular aluminium nanojunction fluxonium qubit, *Nature Materials* **22**, 194 (2023).
- [45] N. Bachar, S. Lerer, S. Hacoheh-Gourgy, B. Almog, and G. Deutscher, Kondo-like behavior near the metal-insulator transition of nanoscale granular aluminum, *Phys. Rev. B* **87**, 214512 (2013).
- [46] U. S. Pracht, T. Cea, N. Bachar, G. Deutscher, E. Farber, M. Dressel, M. Scheffler, C. Castellani, A. M. García-García, and L. Benfatto, Optical signatures of the superconducting Goldstone mode in granular aluminum: Experiments and theory, *Phys. Rev. B* **96**, 094514 (2017).
- [47] F. Levy-Bertrand, T. Klein, T. Grenet, O. Dupré, A. Benoît, A. Bideaud, O. Bourrion, M. Calvo, A. Catalano, A. Gomez, J. Goupy, L. Grünhaupt, U. v. Luepke, N. Maleeva, F. Valenti, I. M. Pop, and A. Monfardini, Electrodynamics of granular aluminum from superconductor to insulator: Observation of collective superconducting modes, *Phys. Rev. B* **99**, 094506 (2019).
- [48] F. Yang, T. Gozdzinski, T. Storbeck, L. Grünhaupt, I. M. Pop, and W. Wulfhchel, Microscopic charging and in-gap states in superconducting granular aluminum, *Phys. Rev. B* **102**, 104502 (2020).
- [49] C. Eichler, Y. Salathe, J. Mlynek, S. Schmidt, and A. Wallraff, Quantum-limited amplification and entanglement in coupled nonlinear resonators, *Phys. Rev. Lett.* **113**, 110502 (2014).
- [50] P. Winkel, I. Takmakov, D. Rieger, L. Planat, W. Hasch-Guichard, L. Grünhaupt, N. Maleeva, F. Foroughi, F. Henriques, K. Borisov, J. Ferrero, A. V. Ustinov, W. Wernsdorfer, N. Roch, and I. M. Pop, Nondegenerate parametric amplifiers based on dispersion-engineered josephson-junction arrays, *Phys. Rev. Appl.* **13**, 024015 (2020).
- [51] D. Rieger, S. Günzler, M. Spiecker, A. Nambisan, W. Wernsdorfer, and I. M. Pop, Fano Interference in Microwave Resonator Measurements, *Phys. Rev. Appl.* **20**, 014059 (2023).
- [52] I. Takmakov, *Minimizing the discrimination time for quantum states of an artificial atom*, Ph.D. thesis, Karlsruhe Institut für Technologie (KIT) (2022), 47.12.01; LK 01.
- [53] D. Sarchi, I. Carusotto, M. Wouters, and V. Savona, Coherent dynamics and parametric instabilities of microcavity polaritons in double-well systems, *Phys. Rev. B* **77**, 125324 (2008).
- [54] T. Hönigl-Decrinis, R. Shaikhaidarov, S. E. de Graaf, V. N. Antonov, and O. V. Astafiev, Two-Level System as a Quantum Sensor for Absolute Calibration of Power, *Phys. Rev. Appl.* **13**, 024066 (2020).
- [55] S. Günzler, P. Winkel, D. Rieger, K. Borisov, M. Spiecker, A. V. Ustinov, I. M. Pop, and W. Wernsdorfer, Superconducting microwave magnetometer for absolute flux detection, *arXiv* (2021), 2107.05929.
- [56] N. E. Frattini, U. Vool, S. Shankar, A. Narla, K. M. Sliwa, and M. H. Devoret, 3-wave mixing Josephson dipole element, *Applied Physics Letters* **110** (2017).
- [57] N. E. Frattini, V. V. Sivak, A. Lingenfelter, S. Shankar, and M. H. Devoret, Optimizing the Nonlinearity and Dissipation of a SNAIL Parametric Amplifier for Dynamic Range, *Phys. Rev. Appl.* **10**, 054020 (2018).
- [58] V. V. Sivak, S. Shankar, G. Liu, J. Aumentado, and M. H. Devoret, Josephson array-mode parametric amplifier, *Phys. Rev. Appl.* **13**, 024014 (2020).
- [59] Technical datasheet: Low noise amplifier LNF-LNC0.3-14A 1078Z. url = <https://quantummicrowave.com/product/0-3-14-ghz-cryogenic-low-noise-amplifier>.
- [60] C. M. Caves, Quantum limits on noise in linear amplifiers, *Phys. Rev. D* **26**, 1817 (1982).
- [61] D. Bothner, T. Gaber, M. Kemmler, D. Koelle, and R. Kleiner, Improving the performance of superconducting microwave resonators in magnetic fields, *Applied Physics Letters* **98** (2011).
- [62] J. Kroll, F. Borsoi, K. van der Enden, W. Uilhoorn, D. de Jong, M. Quintero-Pérez, D. van Woerkom, A. Bruno, S. Plissard, D. Car, E. Bakkers, M. Cassidy, and L. Kouwenhoven, Magnetic-field-resilient superconducting coplanar-waveguide resonators for hybrid circuit quantum electrodynamics experiments, *Phys. Rev. Appl.* **11**, 064053 (2019).
- [63] V. Sivak, N. Frattini, V. Joshi, A. Lingenfelter, S. Shankar, and M. Devoret, Kerr-free three-wave mixing in superconducting quantum circuits, *Phys. Rev. Appl.* **11**, 054060 (2019).
- [64] A. Miano, G. Liu, V. V. Sivak, N. E. Frattini, V. R. Joshi, W. Dai, L. Frunzio, and M. H. Devoret, Frequency-tunable Kerr-free three-wave mixing with a gradiometric SNAIL, *Applied Physics Letters* **120** (2022).
- [65] O. Naaman, D. Ferguson, A. Marakov, M. S. Khalil, W. F. Koehl, and R. J. Epstein, High saturation power josephson parametric amplifier with ghz bandwidth, 2019 IEEE MTT-S International Microwave Symposium (IMS), 259 (2017).
- [66] F. Levy-Bertrand, T. Klein, T. Grenet, O. Dupré, A. Benoît, A. Bideaud, O. Bourrion, M. Calvo, A. Catalano, A. Gomez, J. Goupy, L. Grünhaupt, U. v. Luepke, N. Maleeva, F. Valenti, I. M. Pop, and A. Monfardini, Electrodynamics of granular aluminum from superconductor to insulator: Observation of collective superconducting modes, *Phys. Rev. B* **99**, 094506 (2019).
- [67] S. Probst, F. B. Song, P. A. Bushev, A. V. Ustinov, and



- M. Weides, Efficient and robust analysis of complex scattering data under noise in microwave resonators, *Rev. Sci. Instrum.* **86** (2015).
- [68] G. Stan, S. B. Field, and J. M. Martinis, Critical Field for Complete Vortex Expulsion from Narrow Superconducting Strips, *Phys. Rev. Lett.* **92**, 097003 (2004).
- [69] O. Astafiev, A. M. Zagoskin, A. A. Abdumalikov, Jr., Yu. A. Pashkin, T. Yamamoto, K. Inomata, Y. Nakamura, and J. S. Tsai, Resonance Fluorescence of a Single Artificial Atom, *Science* **327**, 840 (2010).
- [70] J. Y. Mutus, T. C. White, R. Barends, Y. Chen, Z. Chen, B. Chiaro, A. Dunsworth, E. Jeffrey, J. Kelly, A. Megrant, C. Neill, P. J. J. O'Malley, P. Roushan, D. Sank, A. Vainsencher, J. Wenner, K. M. Sundqvist, A. N. Cleland, and J. M. Martinis, Strong environmental coupling in a Josephson parametric amplifier, *Appl. Phys. Lett.* **104** (2014).
- [71] L. Grünhaupt, U. von Lüpke, D. Gusenkova, S. T. Skacel, N. Maleeva, S. Schlör, A. Bilmes, H. Rotzinger, A. V. Ustinov, M. Weides, and I. M. Pop, An argon ion beam milling process for native AlOx layers enabling coherent superconducting contacts, *Appl. Phys. Lett.* **111** (2017).
- [72] Technical datasheet: QCage.24 qubit chip carrier system. url = <https://www.quantum-machines.co/products/qcage>.